ICAS 2021 SHANGHAI
International Council of the Aeronautical Sciences
32nd Congress of the International Council of the Aeronautical Sciences
September 6-10, 2021
Pudong Shangri-La, Shanghai, China

DYNAMIC TRAILING-EDGE FLAP MOVEMENT AS A NON-CONVENTIONAL AERODYNAMIC LIFT MECHANISM

Bremm, Martin[1], Stephan, Ralph[1], Hörnschemeyer, Ralf[1] & Stumpf, Eike[1]

[1]Institute of Aerospace Systems, RWTH Aachen Wuellnerstr. 7, 52062 Aachen, Germany

Abstract

This article analyses a non-conventional aerodynamic lift mechanism that is described in the literature but yet not fully understood. The mechanism shown and discussed in this article enhances the lift of an aerofoil beyond static conditions due to a harmonically oscillating trailing-edge flap. Numerical simulations and experiments in a water tunnel have been conducted to study the lift enhancement mechanism. In the experimental approach, on the one hand, lift and drag forces were measured with a balance, on the other hand, time-averaged and phase-averaged flow fields were captured by means of Particle Image Velocimetry. The results show an increase in the time-averaged lift coefficient with increasing flap oscillation frequency. It has been shown, that reattachment of a separated boundary layer or the delay of boundary layer separation due to an oscillating flap is not mandatory for the lift increase in the context of the discussed flow phenomenon. The real cause still needs to be identified and further research is recommended.

Keywords: unsteady aerodynamics, oscillating flap, lift enhancement

1. Introduction

Pre-COVID aviation is responsible for around 2.5 % of global anthropogenic CO_2 emissions [1]. Although the number of global daily flights has dropped by 70 % and the european daily flights by 90 % [2], the IATA forecasted the annual number of passengers of 2019 will be reached again in 2025 [3]. It can therefore be assumed that the collapse of flights caused by the COVID pandemic is limited in time and that the previous level will be reached again. As before, to meet the ACARE Flightpath 2050 [4] reduction target emissions, it is necessary to pursue all promising research paths. One major pathway is to increase aircraft efficiency.

RWTH Aachen University and TU Munich cooperate on investigating two concepts on a fundamental basis and on exploring the design space for respective technology implementation into current airliners. This work is realised within the research project BIMOD, funded by the German Aeronautic Research Program LuFo V-3 and described in [5], that provides a novel approach combining modern system components to achieve two different effects with one mechanism of action. These are on the one hand, to further reduce weight by increasing the lift coefficient of smaller and lighter high-lift systems and on the other hand, decreasing the separation distances between aeroplanes by excitation of wake vortex instabilities.

This article deals with the increase of the lift coefficient and therefore analyses a non-conventional aerodynamic lift mechanism that is described in the literature but not yet fully understood. The mechanism shown and discussed in this article enhances the lift of an aerofoil beyond static conditions due to a harmonically oscillating trailing-edge flap. Because of the motion of the flap the flow field variables are a function of both spatial location and time, the flow is unsteady [6].

The common parameter used for unsteady aerodynamics is the Strouhal number [7]. This dimensionless parameter represents a dimensionless frequency and is defined as

$$\mathrm{St} = \frac{fl}{U_\infty}, \tag{1}$$

where U_∞ is the freestream velocity, f is the characteristic frequency and l is a characteristic length. For the case of an oscillating flap, a modified reduced frequency

$$f^*_{mod} = \frac{\pi f s}{U_\infty} \tag{2}$$

was introduced by Greenhalgh [8]. Here, f is the flapping frequency and the characteristic length s is the stroke height of the trailing-edge. The latter results from the geometric relationship

$$s = 2\sin(\hat{\eta})c_F, \tag{3}$$

with the flap amplitude $\hat{\eta}$ and the flap chord c_F. The third definition of a dimensionless frequency is given as

$$k = \frac{\pi f c}{U_\infty}. \tag{4}$$

Here, c is the chord of a pitching aerofoil. This reduced frequency is widely used in the discussion of flutter data and has already been used in the early days of investigating unsteady aerodynamics by [9] and [10]. It also has been adapted for unsteady flow phenomena of an oscillating trailing-edge flap by [11] and [12]. In contrast to the modified reduced frequency proposed by Greenhalgh, k does not account for the effect of a change in flap amplitude. Since only one amplitude is investigated in this study, it was decided to use the reduced frequency k as the dimensionless frequency. Referring to Greenhalghs article [8], with the flap chord being 14.5 % of the aerofoil chord and the flap amplitude $\hat{\eta}$ = 12°, the dimensionless frequencies can be converted as

$$k = \frac{f^*_{mod}}{0.06}. \tag{5}$$

This expression will be used, when comparing the reduced frequency with the modified reduced frequency used by Greenhalgh.

Investigations on the lift increase due to an oscillating flap are rarely described in the literature. A more frequently investigated case is flap oscillation that cause an unsteady behaviour of the lift over time but where the steady lift equals the time-averaged lift. Such a case was studied by means of indicial-function concepts [11]. A computational method was applied, with the assumption that the unsteady problem is governed by the linearised partial differential equation and linearised boundary conditions. This method is based on the classical unsteady aerofoil theory already used by von Kármán and Sears [9] and Theodorsen [10]. Non-linear effects, i.e. boundary layer separation, are neglected. The results show a decrease in the lift amplitude with increasing reduced frequency [11]. However, the time-averaged lift remains constant with increasing reduced frequency. As expected from the linear method used in that case, the lift oscillates around a constant mean value. A phase shift of the lift coefficient was observed. For reduced frequencies up to k = 0.6 the results show a phase lag of the lift coefficient and for higher reduced frequencies a phase lead of the lift coefficient.

A recent study that analysed the unsteady aerodynamics of an oscillating trailing-edge flap by means of Leishmans method and experiments conducted in a wind tunnel with a load cell balance indicates the influence of non-linear effects in the unsteady cases [12]. The flap oscillation with an amplitude of $\hat{\eta}$ = 10° at a reduced frequency of k = 0.12 increases the mean lift by 7.4% compared to its quasi-steady case. Higher frequencies were not investigated.

A more detailed investigation of the unsteady lift enhancement with balance measurements conducted in a frequency range from k = 0 to k = 7.96 and flow visualisations at a frequency of k = 12.1 are described in [8]. In that study, an increase of the lift coefficient with an oscillating trailing-edge flap was observed. The lift polars, shown in Figure 1 on the left-hand side, indicate an increase of the maximum lift due to flap oscillation of 55% at high angles of attack. This lift increase was achieved with a flap oscillation frequency corresponding to a reduced frequency of k = 4.48. The typical flow pattern observed at a reduced frequency of k = 12.1 are shown in Figure 1 on the right-hand side. Below the angle of attack of α = 14° (i.e. α = 0° and α = 10°) the vortex street consists of vortex pairs of clockwise and anti-clockwise rotating vortices. With a higher angle of attack, the clockwise rotating

vortex becomes very small and a major change in the vortex pattern was observed between an angle of attack of α = 14.5° and α = 16°. At α = 18° the vortex street consists of single anti-clockwise rotating vortices.

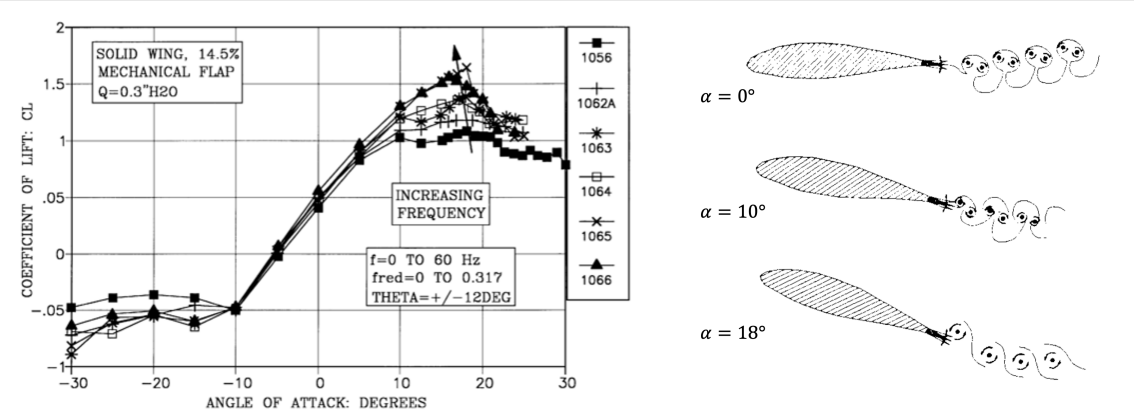

Figure 1 – Lift coefficient vs angle of attack with oscillating flap for ten test runs no. 1056 (k = 0), no. 1062A (k = 2.06), no. 1063 (k = 2.64), no. 1064 (k = 3.52), no. 1065 (k = 4.40) and no. 1066 (k = 5.28) on the left-hand side and the sketched vortex pattern on the right-hand side. [8]

Greenhalgh explains the lift increase over its static conditions by a delay of boundary layer separation on the upper surface. However, further research was recommended to gain more understanding of the unsteady phenomenon and the underlying physics [8]. Computational Fluid Dynamics (CFD) and more experimental studies with better flow visualisation were suggested. The research culminated in a U.S. Patent from 1999 [13].

These findings lead to the following three research questions. First, what influence does the flap oscillation frequency have on the lift coefficient? Second, does the flap oscillation delay the boundary layer separation on the upper aerofoil surface? And third, which vortex formation is observed when the aerodynamic lift is enhanced due to an oscillating flap? This study follows a numerical approach for a wider parameter range and an experimental approach for detailed investigations. The emphasis is on the lift coefficient and the vorticity in the proximity of the aerofoil.

2. Numerical Approach

This section describes the numerical approach, which was carried out in a larger parameter range than the experimental investigations, in order to obtain an overview and to set the parameters for the experiments.

2.1 Geometry

Both, the numerical and the experimental approach uses the same two-dimensional geometry. This geometry, sketched in Figure 2, is a NACA 2412 aerofoil with a plain flap at the trailing-edge. The nomenclature in context to the aerofoil geometry is used throughout this study. As it can be seen in the figure, $\bar{\eta}$ is the mean flap angle, $\hat{\eta}$ is the flap amplitude and the distance s is the stroke height of the oscillating trailing-edge. The overall chord c of the aerofoil has a length of 150 mm with the flap hinge at 80 %. Between the main wing and the flap is a gap of 0.5 mm.

2.2 Numerical Setup

The applied computational mesh was generated with CENTAUR. It is a hybrid 2D-mesh with a layer of quads at the aerofoil and triangles to the far field. The dimensionless wall distance is set to $y^+ < 1$. The computational domain and the mesh close to the aerofoil is shown in Figure 3. The farfield dimension is 100 times the chord length of the aerofoil to minimise the influence of the far field on the near flow field. The boundary conditions are set to velocity inlet on the left-hand side, pressure outlet on the right-hand side and velocity inlet/pressure outlet at the top and at the bottom. For the transient simulations of the oscillating flap, the mesh is adapted dynamically for each time step. A user defined

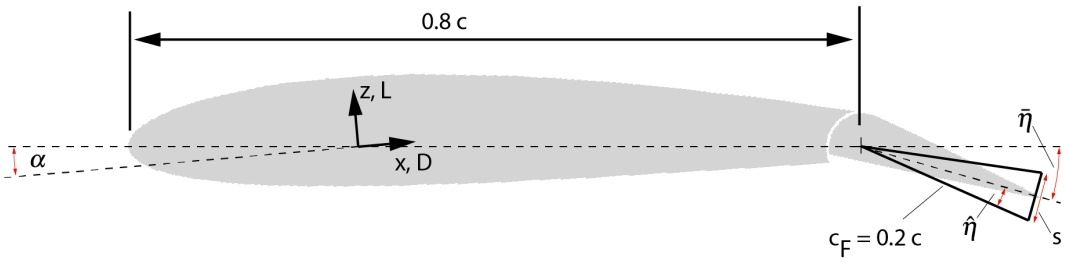

Figure 2 – Geometry and nomenclature of the aerofoil with trailing-edge flap.

function (UDF), based on the flap amplitude $\hat{\eta}$, the reduced frequency k, the freestream velocity U_∞, the chord c and the time t, is implemented as:

$$g(t) = \hat{\eta} \sin(\frac{2kU_\infty}{c}t). \tag{6}$$

A more detailed description of the UDF for dynamic mesh motion methods can be found in [14].

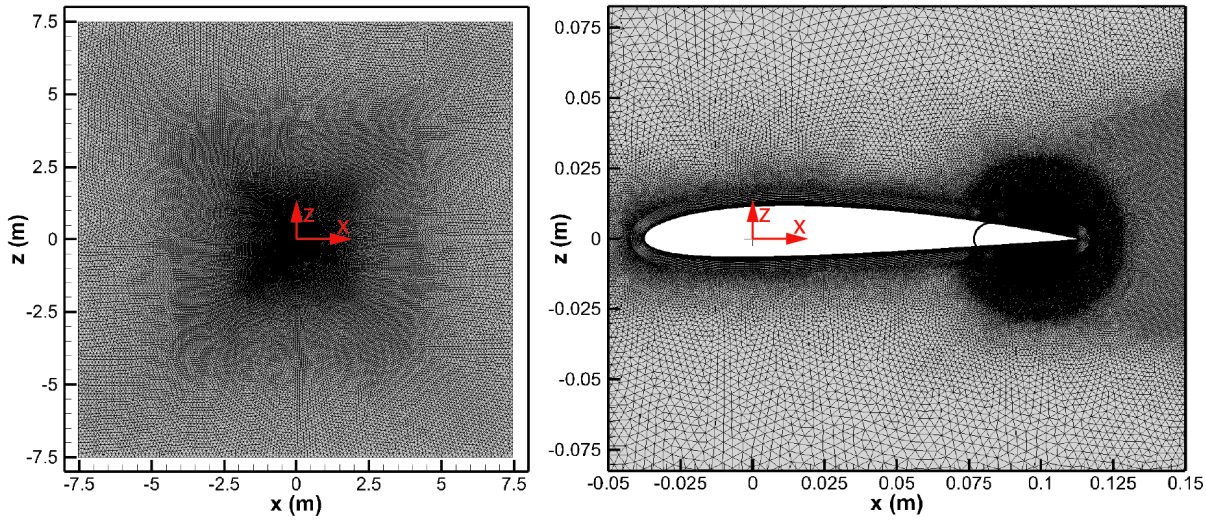

Figure 3 – Computational domain with the boundaries and the computational mesh close to the aerofoil.

The parameters used in this study are angle of attack α, amplitude $\hat{\eta}$, mean flap angle $\bar{\eta}$ and reduced frequency k. All parameter combinations simulated are given in Table 1. At the highest frequency, only one mean flap angle was simulated, as a higher frequency increases the computation time. The fluid properties of water were used for the numerical simulations, since the experimental investigations are also carried out in water. The boundary layer is modelled with a natural laminar-turbulent transition. The Reynolds number was fixed at Re_c = 0.3x10^6, with a freestream velocity of 2 m/s, a chord length of 150 mm and a water temperature of 20 °C.

Table 1 – Parameters of the conducted CFD simulations.

Parameter:	α	$\bar{\eta}$	$\hat{\eta}$	k
Transient (300 timesteps)	0°, 5°, 14°	0°, 2°, 4°, 6°, 8°	2°	0.0025, 0.25, 0.5, 0.75
Transient (1500 timesteps)	0°, 5°, 14°	2°	2°	5.11

The computational fluid dynamics (CFD) is simulated by ANSYS Fluent 2019 R3. The unsteady Reynolds-averaged Navier-Stokes equations (URANS) are solved by means of a pressure based solver described in [15]. The turbulence is implied by a 2-equation turbulence model SST-k-ω that is standard for such kind of application, see e.g. [14].

2.3 Results of the CFD Simulations

The time-averaged lift and drag values are plotted in Figure 4 and clearly show the influence of the angle of attack and flap deflection angle. For reasons of clarity the different oscillation frequencies are plotted with the same marker symbol for each flap deflection angle, as they overlap. The influence of the oscillation frequency is hardly visible in this plot, at least for the range up to a reduced frequency of k = 0.75. Only for the highest reduced frequency (k = 5.11) at $\bar{\eta}$ = 2°, an effect is visible and becomes even more evident with a higher angle of attack. For all three angles of attack, the lift coefficient increases with the oscillation frequency.

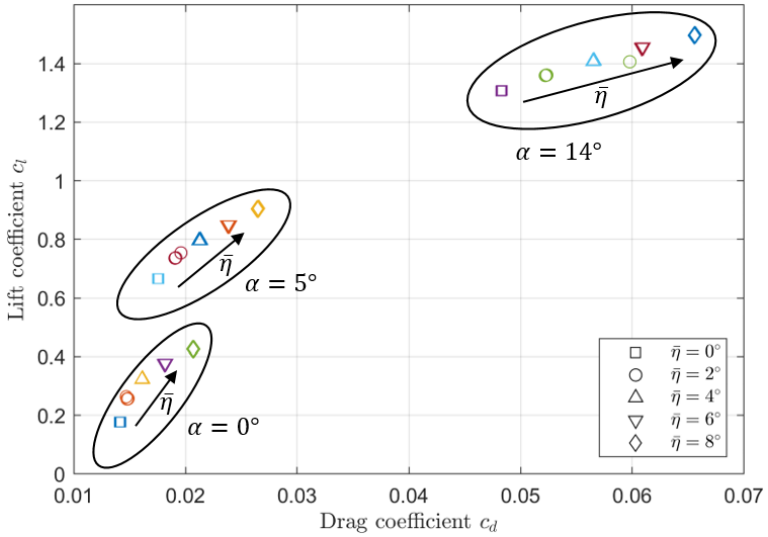

Figure 4 – Lift to drag diagram of the time-averaged results for all conducted CFD simulations, all frequencies are plotted with the same marker symbol for each flap deflection angle.

For a detailed analysis of the vortex formations and the influence of the flap oscillation frequency on the lift and drag coefficients, an experimental approach is chosen.

3. Experimental Approach

This section describes the experimental approach of the conducted experiments. First, the experimental setup is described, followed by a description of the measurement methodologies.

3.1 Flow Facility and Test Model

The experiments were conducted in the water tunnel facility (Figure 5) of the RWTH Aachen University which is a circulating tunnel with a closed test section of 0.54 m x 0.54 m and a characteristic turbulence level of 2 % - 3 %. The tunnel with a contraction ratio of 1.85 can run at flow speeds from 0 m/s - 4 m/s. All experiments of this study are conducted at a Reynolds number of Re_c = 0.3x10^6. Since the flap frequency is linked to the flow velocity via the dimensionless frequency, see Eq. (4), it is beneficial to keep the flow velocity as low as possible. With the water heated up to a temperature of 40 °C, the freestream velocity could be set to 1.32 m/s.

The test model is identical to the geometry used in the simulations, see section 2. Its aspect ratio Λ is 3 and the chord c has a length of 150 mm. The wing was manufactured of an aluminium alloy with high stiffness, to avoid bending. The gaps between the wing and the side walls were reduced to a minimum of 0.1 mm to reduce the three-dimensional wake vortex to a minimum while still enabling force measurements.

On both sides along the leading-edge a transition trip of a distributed roughness was used, to guarantee a fully turbulent boundary layer. The laminar-turbulent transition correlates with the Reynolds number Re_h, which is related to the height of the transition trip. A fully turbulent boundary layer for the transition trip of distributed roughness with a Reynolds number of Re_h = 600 was experimentally proven by Braun [16]. Therefore, the height of the transition trip for this experimental setup is between 200 µm to 355 µm.

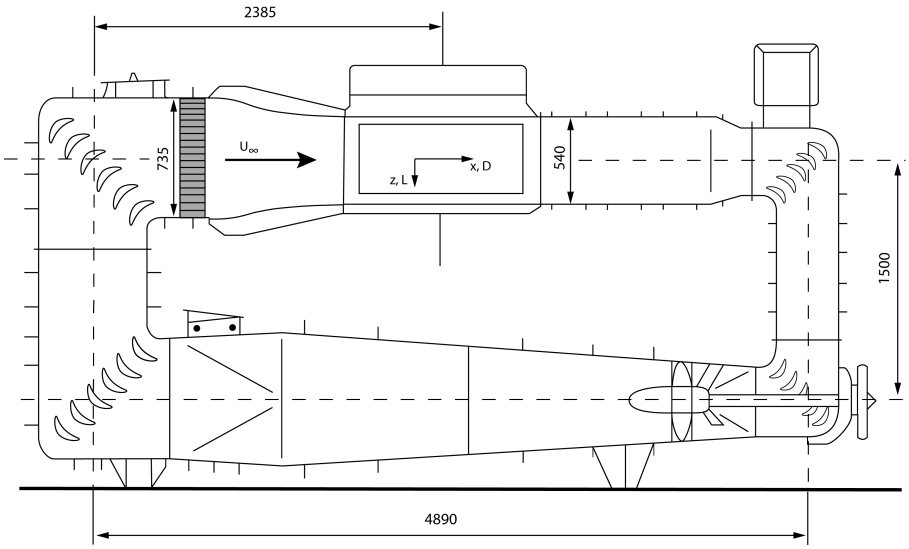

Figure 5 – Water tunnel of the RWTH Aachen University.

The kinematics for the flap actuation, depicted in Figure 6, are positioned outside of the test section and are connected to the test model via rods. The electric motor drives an eccentric shaft that is linked with a slider-crank mechanism to the oscillating shaft. With this kinematic, the three parameters oscillation frequency, flap amplitude and mean flap angle are independently adjustable.

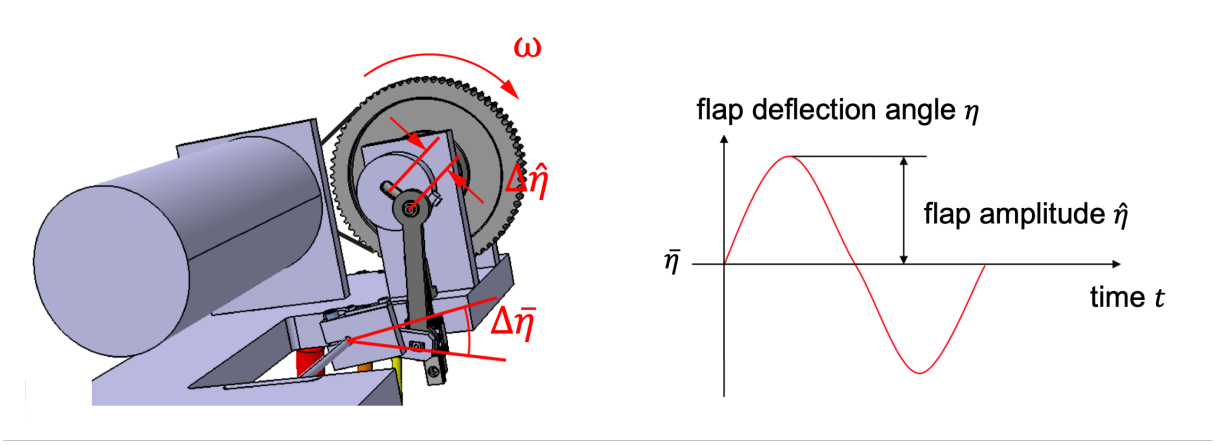

Figure 6 – Kinematics for flap actuation and one period of flap deflection angle over time.

For this research, two different measurement methods shown in Figure 7 were used. First, a balance was used to measure the lift and drag forces. Second, triggered Particle Image Velocimetry (triggered-PIV) was used to measure the flow field synchronized to the flap frequency. The angle of attack was varied from 0° to 18° for the steady state test cases and held constant at 5° and 14° for the unsteady test cases (flap oscillation at $\bar{\eta}$ = 2° with an amplitude of $\hat{\eta}$ = 2°). During the load measurements, the reduced frequency was varied in the unsteady test cases between k = 0.0025 and k = 5.5 which corresponds to oscillating frequencies between 0.07 Hz and 15.37 Hz. For the PIV measurements, the reduced frequency is fixed at k = 5.11 which corresponds to an oscillating frequency of 14.29 Hz.
Two cases with a moderate angle of attack (α = 5°) and with a maximum angle of attack (α = 14°) are further investigated in the experimental approach. Table 2 lists the used parameters of the conducted experiments.

3.2 Lift and Drag Measurements

In the first experimental setup, the lift and drag forces were measured with an external six-component balance. The load cell of the balance is shown in Figure 7 on the left. The model is mounted

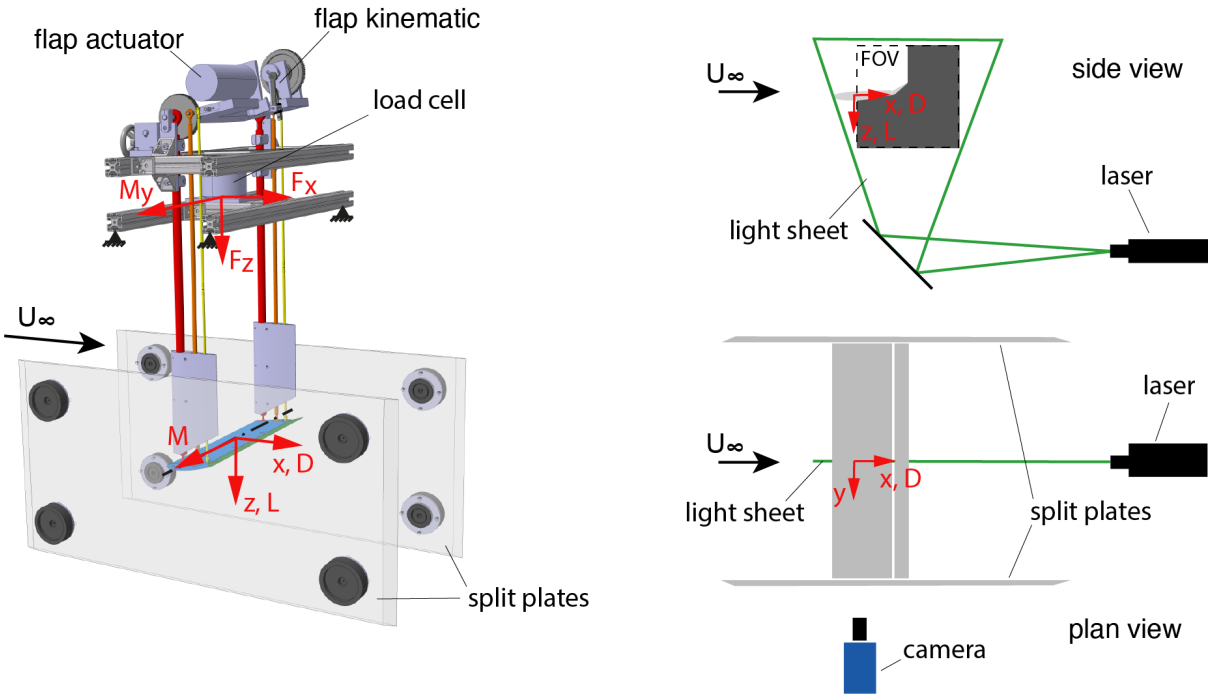

Figure 7 – Experimental setup for the measurements of lift and drag (left) and triggered PIV (right).

Table 2 – Parameters of the conducted experiments.

Parameter:	α	$\bar{\eta}$	$\hat{\eta}$	k
PIV (steady)	5°, 14°	0°	-	-
Triggered PIV (unsteady)	5°, 14°	2°	2°	5.11
Balance (steady)	0° - 18° (1°-steps)	2°	-	-
Balance (unsteady)	5°, 14°	2°	2°	0.025, 0.25, 0.5, 1, 1.5, 2, 2.5, 3, 3.5, 4, 4.5, 5, 5.11, 5.5

upside down, so the lift force is directed downwards, and the drag force is directed in flow direction. The balance of type K6D110 from ME-Meßsysteme allowed an acquisition frequency of 20 kHz. In addition to the aerodynamic forces, the balance was also affected by the vibrations from the flow facility. The vibration frequencies depend on the flow speed and lie in a spectrum of 28 Hz to 40 Hz. Therefore, a low pass filter was applied to the data in post-processing, where the cut-off frequency was proportional to the flap oscillation. The load results within this study always represent the time-average of the lift respectively drag forces calculated according to

$$\bar{F} = \frac{1}{T}\int_{t_1}^{t_2} F(t)dt. \tag{7}$$

Here, F represents a force value and T is the period of a test run starting at t_1 and ending at t_2.

3.3 Particle Image Velocimetry Measurements

A second experimental setup was used for the triggered-PIV measurements. Figure 7 (right) depicts schematically the PIV setup and the field of view (FOV). The Nd:Yag laser Quantel Twins Ultra CFR 200 was positioned below the test section. The pulse separation of the double pulse mode was set to dt = 300 µs, to get a particle shift in the range of 5 to 10 pixels for mean flow velocities. An optical setup of lenses and a planar mirror span a light sheet with a thickness of 2 mm and redirects the laser light in the vertical direction through the lower window into the test section. The light sheet is in midspan position to minimise 3D-effects from the wing side wall boundary layer interaction into the measurement plane. The double-frame camera pco.2000 was positioned with a 90° angle to the flow

direction. The ccd-sensor of the used camera has a resolution of 2048 x 2048 pixels with a dynamic range of 14 bit. The flow was seeded with polyamide particles with a density of 1.183 g/cm^3.
The PIV measurements were triggered at six different flap angles η = [0°, 0.8°, 1.6°, 2.4°, 3.2°, 4°], for both downwards (downstroke) and upwards (upstroke) moving flap. Test runs were carried out for each flap angle separately. In one test run, 300 frames were captured to allow phase-averaging in the post-processing. Therefore, the concept of triple decomposition will be explained briefly. The flow can be decomposed into the steady, the unsteady and the turbulent components. This is known as triple decomposition introduced by Hussain and Reynolds [17]. They defined the flow value U as a superposition of the time-average $\bar{U}$, the cyclic component $\tilde{U}$ and the turbulent component U'

$$U(x,t) = \bar{U}(x) + \tilde{U}(x,t) + U'(x,t) \tag{8}$$

with the spatial variable x and the time variable t. The phase-average is the average of the values of $U(x,t)$ at a particular phase in the cycle of the periodic phenomenon. Since the turbulent component of the phase-average is zero by definition $\langle U' \rangle$ = 0, the phase-average of the flow field consist only of the time-average and the cyclic component

$$\langle U(x,t) \rangle = \bar{U}(x) + \tilde{U}(x,t). \tag{9}$$

The phase-average of an organised wave is defined as

$$\langle U(x,t) \rangle = \lim_{N\to\infty} \frac{1}{N} \sum_{n=0}^{N} U(x, t+n\tau) \tag{10}$$

where τ is the period of the wave and N is the number of cycles. In this case N is equal to the number of frames captured in the PIV measurements for each run, thus Eq. (10) becomes

$$\langle U(x,t) \rangle = \frac{1}{300} \sum_{n=1}^{300} U(x, t+n\tau). \tag{11}$$

The particle-images are processed in pre-processing and post-processing. The processing steps are subtracting sliding background, masking out of the wing and flap inside the FOV and a multi-pass cross-correlation with an interrogation window size of 96 x 96 pixels in the first passes and 24 x 24 pixels in the last passes.

4. Results and Discussion

4.1 Lift and Drag Forces

First, the results of the steady state experiments are evaluated. Figure 8 shows the lift coefficient (left) and drag coefficient (right) over the angle of attack from α = 0° to α = 18° in 1° step size for the flap at η = 2°. The maximum lift coefficient $c_{l,max}$ is at an angle of attack of α = 14°. From an angle of attack of α = 15° the flow over the wing stalls as the drag coefficient diverges.
The lift and drag coefficient of the unsteady experiments with an oscillating flap are discussed hereafter. Figure 9 shows the lift and drag coefficients over the reduced frequency for α = 5° (left) and α = 14° (right). The lift coefficient increases with reduced frequency. The slope of the lift increase depends on the angle of attack. Note, that the lift coefficient for the quasi-steady runs of both cases is different. In contrast to the increase of the lift coefficient, the drag coefficient remains constant over the reduced frequency. A part of this can be explained by the fact, that the lift increase does not cause induced drag, because the side walls suppress wing tip vortices.
Figure 10 shows the change of the lift coefficient over the reduced frequency for the two angles of attack investigated. The change of every unsteady run relates to the quasi-steady run at k = 0.025. In both cases, α = 5° (left) and α = 14°, the lift coefficient increases linearly with the reduced frequency, independent of the angle of attack. Furthermore the slope of the percentage change is similar. As mentioned above, the results reported by [8] only show a lift increase at maximum angles of attack, see Figure 1. In contrast, the increase of the lift coefficient, see 9, is also present at a moderate angle of attack i.e. α = 5°, besides the increase of the lift at maximum angle of attack α_{max}. The maximum lift increase due to flap oscillation found in this study is approx. 9% at a reduced frequency of 5.5.

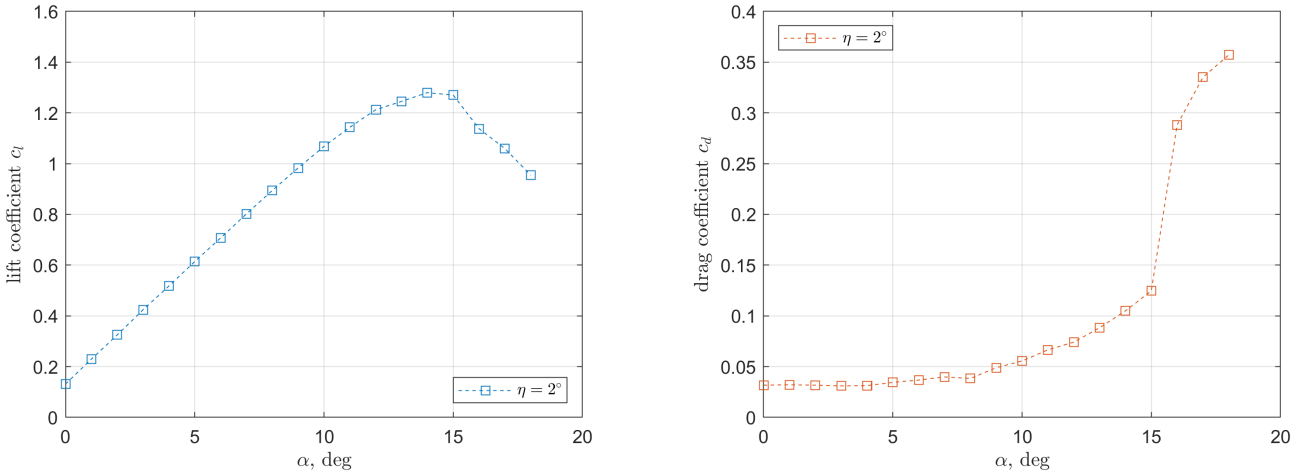

Figure 8 – Polar plots of the lift and drag coefficient for a flap angle of $\eta = 2°$ at steady flow conditions.

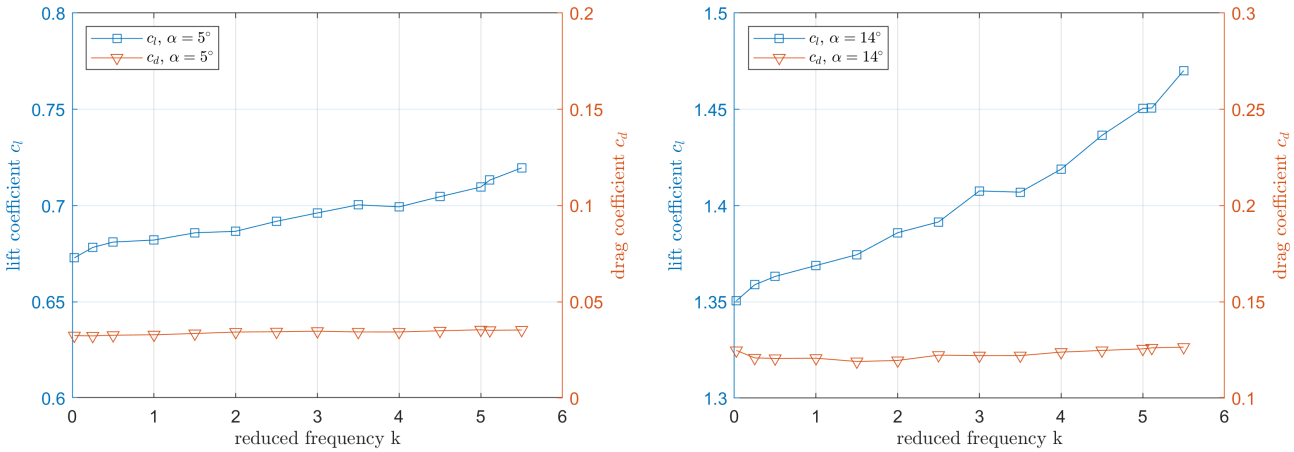

Figure 9 – Lift and drag coefficient over the reduced frequency for an angle of attack $\alpha = 5°$ (left) and $\alpha = 14°$ (right).

This is relatively little compared to the lift increase of 55% reported by [8]. However, that increase of lift was reached with a flap amplitude of $\hat{\eta} = 12°$ compared to the flap amplitude of $\hat{\eta} = 2°$, used in this study.

4.2 Steady State and Unsteady Flow Fields

This section discusses the results gained from the PIV measurements. The flow fields depicted below show the normalised vorticity ω_y in the proximity of the aerofoil. The vorticity rotating in a clockwise direction is shown in red and the vorticity rotating in an anti-clockwise direction is shown in blue. Streamlines are shown as black solid lines.

To start with, the steady-state flow field will be analysed first. Figure 11 shows the steady-state flow fields for the angles of attack $\alpha = 5°$ and $\alpha = 14°$ with the flap at its most upward position $\eta = 0°$. In both cases, a shear layer in the wake of the trailing-edge is clearly visible. The boundary layer is fully attached at an angle of attack of $\alpha = 5°$. This is not the case at an angle of attack of $\alpha = 14°$. Here the boundary layer on the main wing separates at $x/c = 0.64$. At the gap between the wing and the flap, the boundary layer reattaches.

The unsteady flow field is discussed below. Figure 13 to 16 show all contour plots of the phase-averaged flow fields for the oscillating flap for $\alpha = 5°$ and $\alpha = 14°$. The flap is moving downwards to higher flap deflection angles in Figure 13 and Figure 15 and upwards to lower flap deflection angles in Figure 14 and Figure 16. Each figure shows six phase-averaged flow fields at the trigger angles described in section 3.

In both cases ($\alpha = 5°$ and $\alpha = 14°$), a discrete vortex rotating in the anti-clockwise direction is created

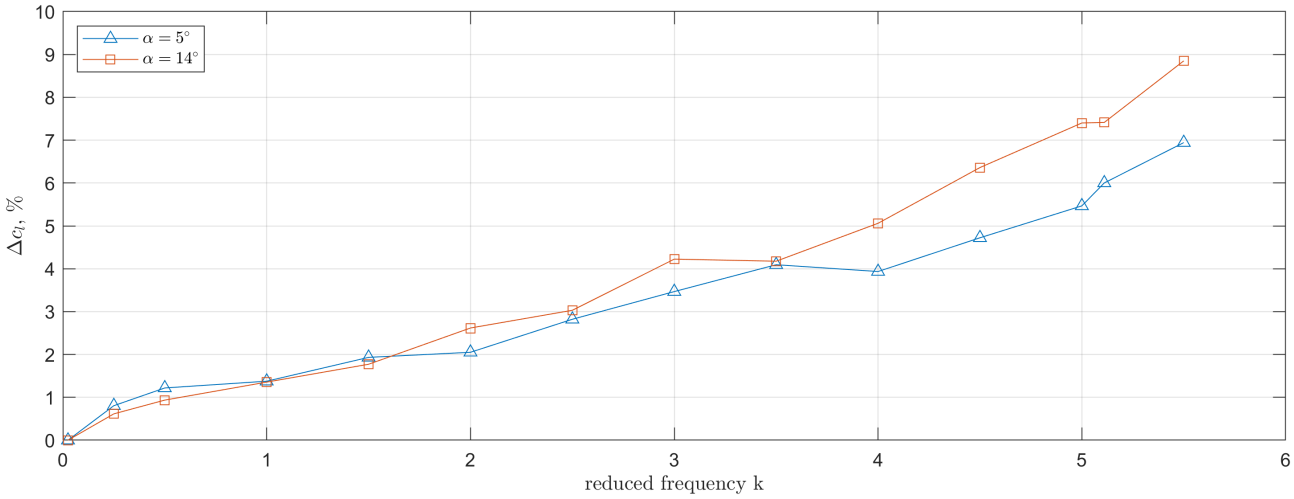

Figure 10 – Change in the lift coefficient Δcl versus the reduced frequency k.

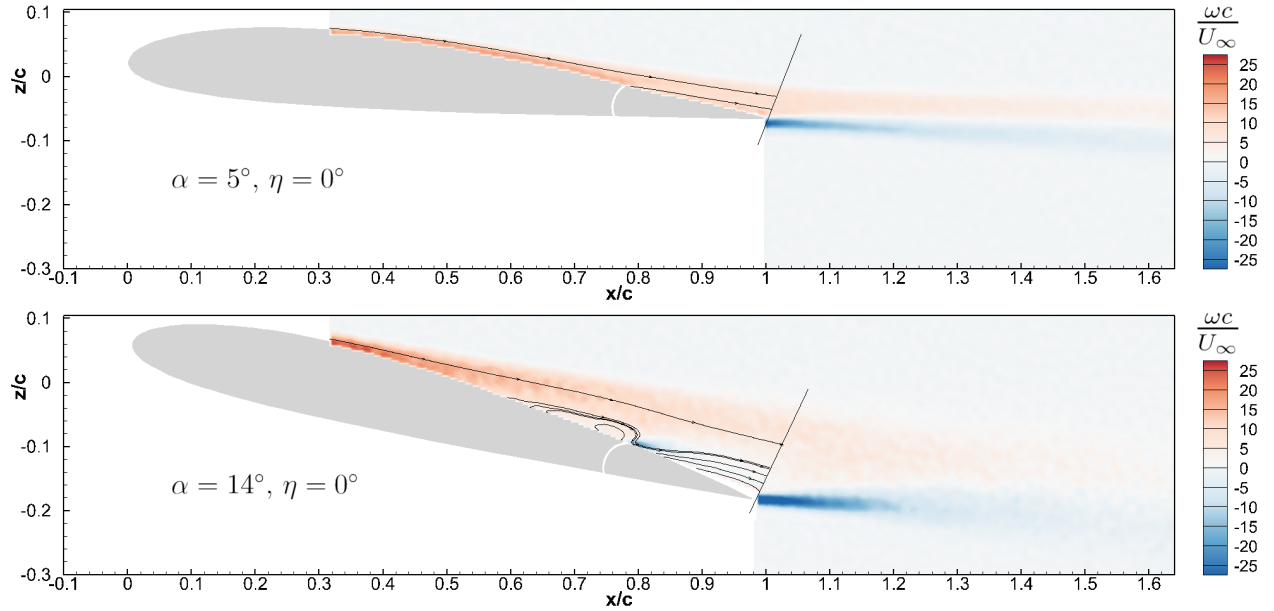

Figure 11 – Time-averaged flow fields of the steady state captured with PIV.

in the wake of the trailing-edge. Before the formation of the discrete vortex, the vorticity increases at the trailing-edge during the downstroke. Qualitatively, a certain level of vorticity must be reached before a discrete vortex is formed. In the first case (α = 5°), this is achieved almost at the most downward position of the flap. In the second case (α = 14°), vortex formation occurs earlier in the oscillation period. Also, the vortex is more pronounced. Right after the vortex is formed, the vortex starts to travel downstream.

Noticeably, the vortex topology described in the literature (see Figure 1) for moderate angles of attack (i.e. α = 0° and α = 10°) distinguishes from the vortex topology at α = 5° shown in this study (Figure 13 and Figure 14). The vortex topology in the literature at moderate angles of attack is composed of counter rotating vortex pairs and is described as ghost like shapes. The investigations made here, always show single anti-clockwise rotating vortices. In the literature, this is only the case for high angles of attack when the lift enhances due to flap oscillation is present. It seems, that an increase in the lift due to flap oscillation is directly related to a chain of single anti-clockwise rotating vortices.

As in the steady state flow fields, the boundary layer at α = 5° and at α = 14° also differ in the unsteady flow fields. In the first case, the boundary layer remains attached even with an oscillating flap. In the second case, the reattached boundary layer follows the flap movement during the downstroke but separates during the upstroke.

In the case of present boundary layer separation on the main wing, the onset of boundary layer separation becomes unsteady with an oscillating flap. Figure 12 shows the position of separation onset over one flap oscillation period and the separation point for the steady state case. The onset of separation slightly moves during the flap oscillation period. At the beginning of the oscillation period, the onset of separation is at x/c = 0.65 and moves downstream during the downstroke of the flap. The most downstream position of the onset of boundary layer separation is reached in the second quarter of the oscillation period. This is when the vortex at the trailing-edge is formed. The beginning of the upstroke of the flap coincides with an upstream shift of the onset of boundary layer separation.

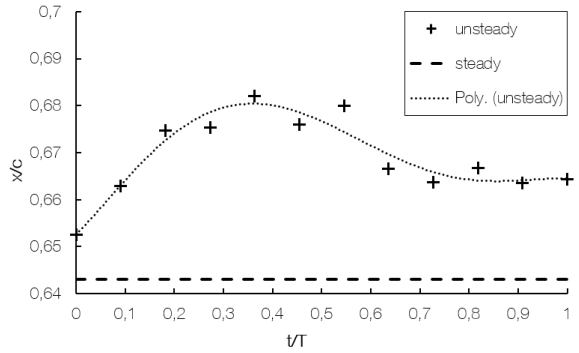

Figure 12 – Onset of boundary layer separation over an oscillation period.

It was proposed, that the lift enhancement due to flap oscillation is caused by reattaching of the boundary layer [8]. The results presented here indicate a lift enhancement independent from the fact whether the boundary layer is attached or separated. Therefore, the assumption that the lift enhancement is caused by reattaching of the boundary layer can be refuted. It should be noted, that the real cause for the lift enhancement beyond static conditions still needs to be identified.

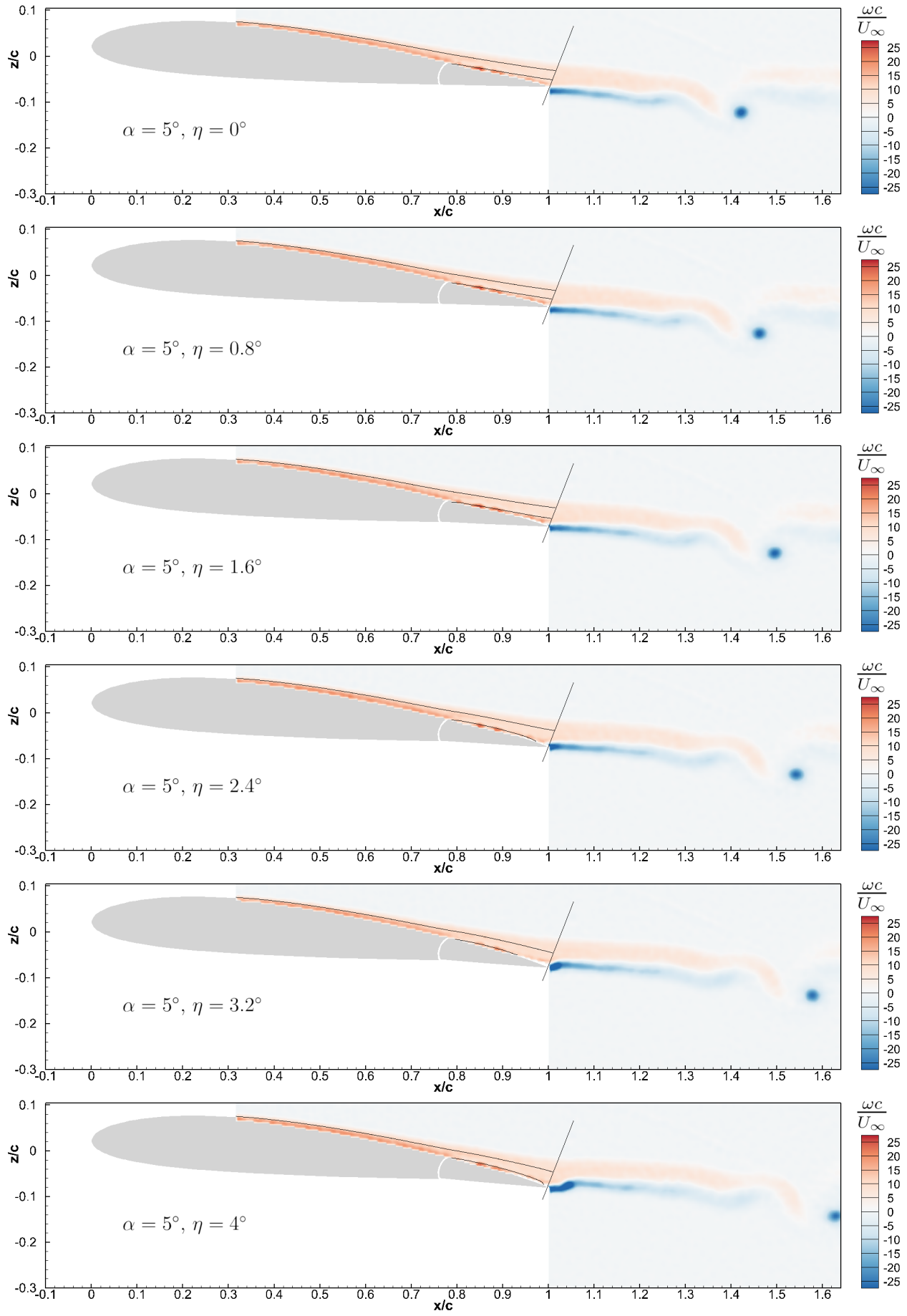

Figure 13 – Phase-averaged flow fields of the flap downstroke with an angle of attack of α = 5° and a reduced frequency of k = 5.11 captured with triggered-PIV.

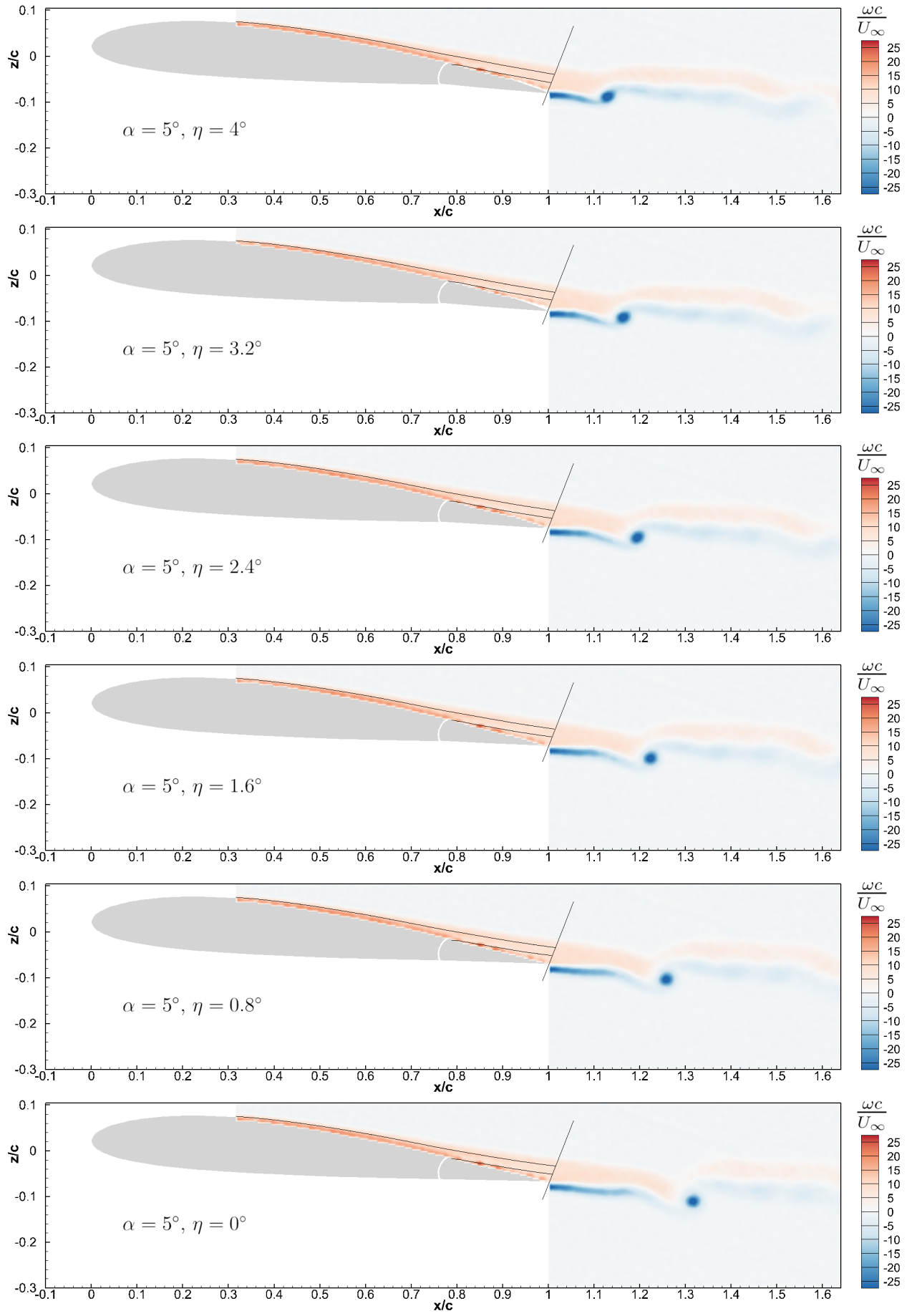

Figure 14 – Phase-averaged flow fields of the flap upstroke with an angle of attack of α = 5° and a reduced frequency of k = 5.11 captured with triggered-PIV.

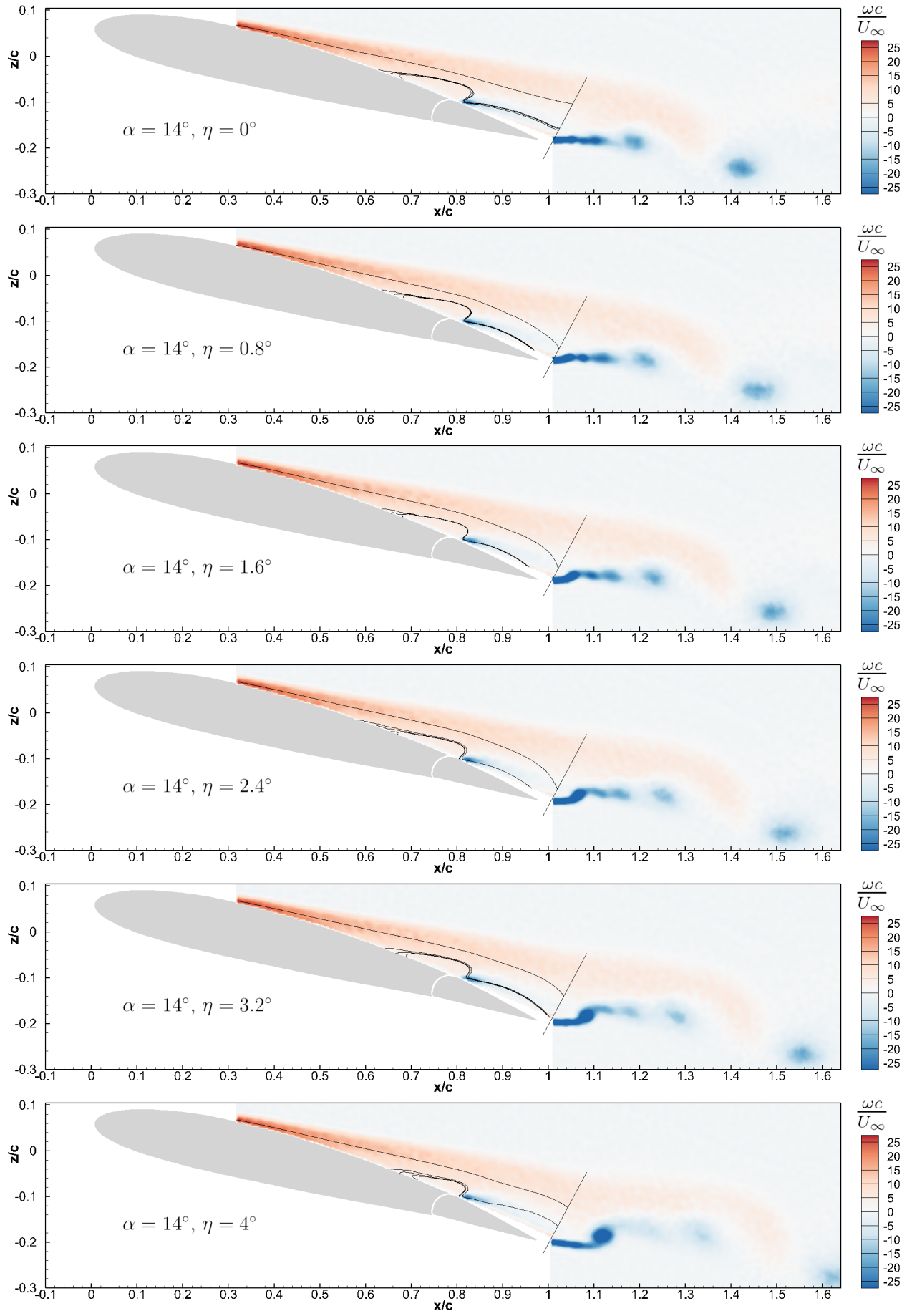

Figure 15 – Phase-averaged flow fields of the flap downstroke with an angle of attack of α = 14° and a reduced frequency of k = 5.11 captured with triggered-PIV.

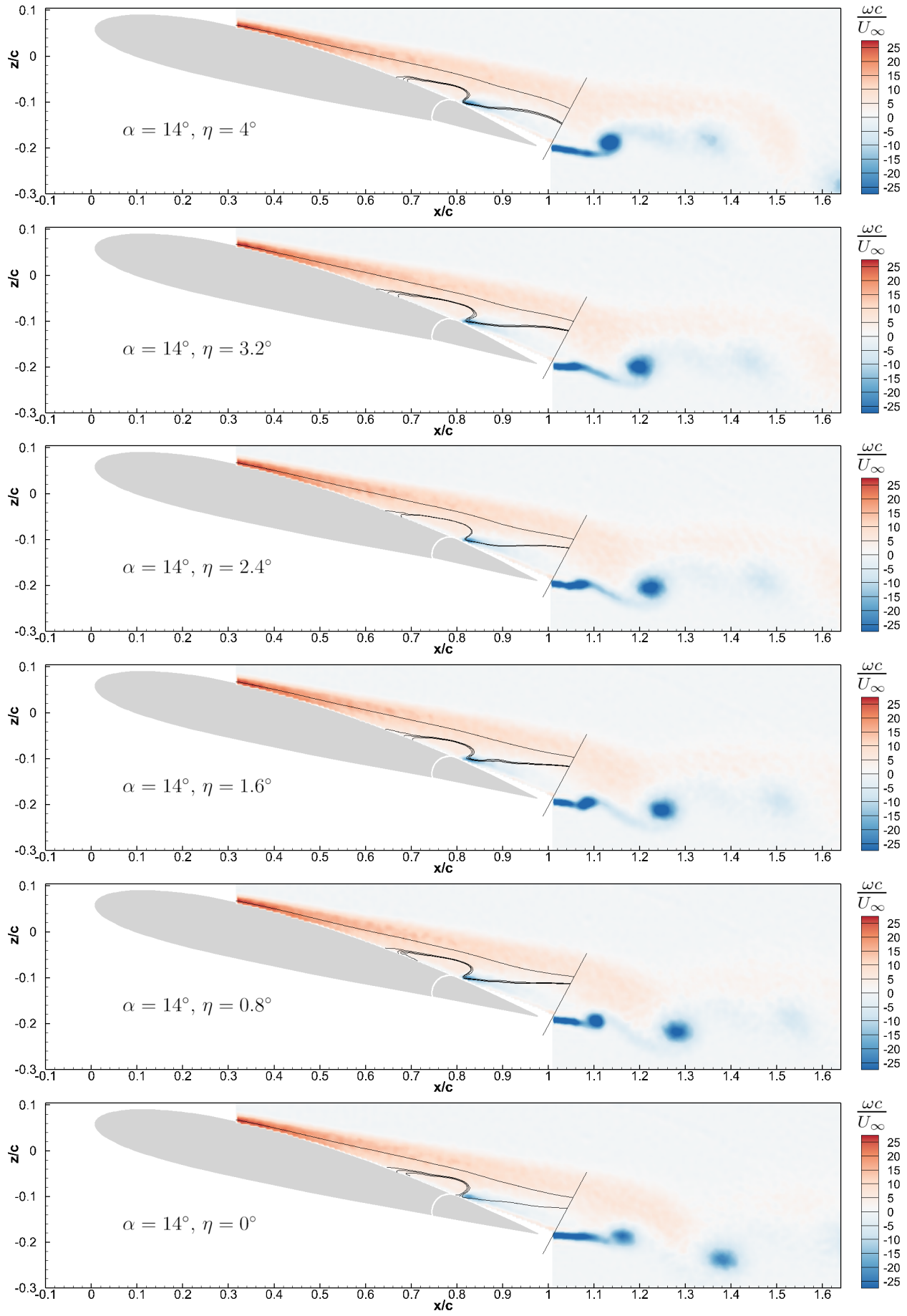

Figure 16 – Phase-averaged flow fields of the flap upstroke with an angle of attack of α = 14° and a reduced frequency of k = 5.11 captured with triggered-PIV.

5. Conclusion

This study deals with an unsteady flow phenomenon that enhances the lift due to a harmonically oscillating trailing-edge flap. As mentioned above, a quite high lift increase of 55% compared to the steady state case is described in the literature. CFD simulations were conducted to get an overview. Therefore, a URANS method with a SST-k-ω turbulence model has been applied on a hybrid 2D-mesh. Experimental investigations were conducted in a water tunnel. The aerodynamic forces (lift and drag) were measured with an external six-component balance and the velocity fields in the midspan position were captured by means of triggered PIV. Three research questions have been formulated for this study:

- First, what influence does the flap oscillation frequency have on the lift coefficient?

A lift enhancement due to flap oscillation was shown at the maximum angle of attack α_{max} as well as at a moderate angle of attack i.e. $\alpha = 5°$. The results show a linear increase of the lift coefficient with increasing in the reduced frequency.

- Second, does the flap oscillation delay the boundary layer separation on the upper aerofoil surface?

In the case that boundary layer separation on the main wing is present, the onset of boundary layer separation becomes unsteady with an oscillating flap and is slightly shifted downstream, compared to the steady state case.

- And third, which vortex formation is observed when the aerodynamic lift is enhanced due to an oscillating flap?

The analysis of the vortex topology has shown, that single anti-clockwise rotating vortices occur in both cases investigated.
The real cause for the lift enhancement beyond static conditions still needs to be identified. Also, different flap amplitudes should be investigated for analysing the effect of flap amplitude on the lift increase. Furthermore, it should be investigated under which conditions counter-rotating vortex pairs or single anti-clockwise rotating vortices occur.

6. Acknowledgements

The funding of this investigation within the LuFo V-3 project BIMOD (Influencing maximum lift and wake vortex instabilities by dynamic flap movement) (FKZ: 20E1702A) by the German Federal Ministry for Economic Affairs and Energy (BMWi), is gratefully acknowledged.

7. Contact Author Email Address

martin.bremm@ilr.rwth-aachen.de

8. Copyright Statement

References

[1] Deutsches Zentrum für Luft- und Raumfahrt (DLR) *Zero Emission Aviation - Emissionsfreie Luftfahrt*. White Paper, DLR, Köln, 2020.

[2] Pearce B. *COVID-19; Wider economic impact from air transport collapse*. IATA Economics, 2020.

[3] Mikosz S. *Net-Zero Carbon Emissions by 2050*. IATA Environment and Sustainability, 2021.

[4] Policy/European Commission *Flightpath 2050: Europe's vision for aviation; maintaining gloabal leadership and serving society's needs; report of the High-Level Group on Aviation Research*. Publ. Off. of the Europ. Union, Luxembourg, 2011.

[5] Stephan R, Bremm M, Hörnschemeyer R, Stumpf E, Schmidt H, Schröder K-U, Ruhland J and Breitsamter C. Influence of Dynamic Flap Movement on Maximum Lift and Wake Vortex Evolution. *68. Deutscher Luft- und Raumfahrtkongress*, Darmstadt, Germany, 2019.

[6] Anderson J D. *Fundamentals of Aerodynamics*. 5st edition, McGraw-Hill, 2011.

[7] Strouhal V. Ueber eine besondere Art der Tonerregung. *Physikalisch-medicinische Gesellschaft*, Würzburg, Germany, pp 216 - 251, 1878.

[8] Greenhalgh S. Lift enhancement due to unsteady aerodynamics. *11th Applied Aerodynamics Conference*, Monterey, CA, USA., pp 1018-1028, 1993.

[9] von Kármán T and Sears W. Airfoil Theory for Non-Uniform Motion. *Journal of the Aeronautical Sciences*, Vol. 5, No. 10, pp 379-390, 1938.

[10] Theodorsen, T. *General Theory of Aerodynamic Instability and the Mechanism of Flutter*. Report No. 496, National Advisory Committee for Aeronautics, 1935.

[11] Leishman J G. Unsteady Lift of a Flapped Airfoil by Indicial Concepts. *Journal of Aircraft*, Vol. 31, No. 2, pp 288-297, 1994.

[12] Shehata H, Zakaria M, Hussein A and Hajj M R. Aerodynamic Analysis of Flapped Airfoil at High Angles of Attack. *2018 AIAA Aerospace Sciences Meeting*, Kissimmee, FL, USA, pp 1-15, 2018.

[13] Greenhalgh S. Oscillating Flap Lift Enhancement Device. *US. Patent*, No. 5,884,872, 1999.

[14] Ruhland J and Breitsamter C. Numerical analysis of high-lift configurations with oscillating flaps. *CEAS Aeronautical Journal*, Vol. 12, pp 345–359, 2021.

[15] ANSYS. *ANSYS Fluent Theory Guide*. Release 17.0., ANSYS, Inc. South-pointe Canonsburg, USA, 2016.

[16] Braun S. *Numerische Simulation von Wirbelaufrollvorgängen an Tragflügeln*. Dissertation, RWTH Aachen University, 2016.

[17] Hussain A and Reynolds W. The mechanics of an organized wave in turbulent shear flow. *Journal of Fluid Mechanics*, Vol. 41, No. 2, pp 241-258, 1970.